

Geophysical Research Letters[®]



RESEARCH LETTER

10.1029/2021GL096113

Oceanic and Atmospheric Drivers of Post-El-Niño Chlorophyll Rebound in the Equatorial Pacific

Hyung-Gyu Lim¹ , John P. Dunne² , Charles A. Stock² , Paul Ginoux² , Jasmin G. John^{2,3} , and John Krasting² 

¹Atmospheric and Oceanic Sciences Program, Princeton University, Princeton, NJ, USA, ²NOAA/OAR/Geophysical Fluid Dynamics Laboratory, Princeton, NJ, USA, ³NOAA/OAR/Atlantic Oceanographic and Meteorological Laboratory, Miami, FL, USA

Key Points:

- The observed post-El Niño chlorophyll anomaly, “chlorophyll rebound,” in the equatorial Pacific is successfully simulated in GFDL-ESM4.1
- This rebound is primarily driven by surfacing high iron anomalies propagated from western Pacific via Equatorial Undercurrent
- High dust-iron deposition anomalies arising from dry land conditions augment the post-El Niño chlorophyll rebound

Supporting Information:

Supporting Information may be found in the online version of this article.

Correspondence to:

H.-G. Lim,
hyunggyu@princeton.edu

Citation:

Lim, H.-G., Dunne, J. P., Stock, C. A., Ginoux, P., John, J. G., & Krasting, J. (2022). Oceanic and atmospheric drivers of post-El-Niño chlorophyll rebound in the equatorial Pacific. *Geophysical Research Letters*, 49, e2021GL096113. <https://doi.org/10.1029/2021GL096113>

Received 24 SEP 2021
Accepted 1 MAR 2022

Author Contributions:

Conceptualization: Hyung-Gyu Lim, Charles A. Stock
Data curation: Charles A. Stock, Jasmin G. John, John Krasting
Formal analysis: Hyung-Gyu Lim
Funding acquisition: John P. Dunne
Methodology: Hyung-Gyu Lim, Charles A. Stock, Paul Ginoux, Jasmin G. John, John Krasting
Project Administration: John P. Dunne
Resources: John P. Dunne, Charles A. Stock, Jasmin G. John
Software: Jasmin G. John, John Krasting

© 2022 The Authors.

This is an open access article under the terms of the [Creative Commons Attribution-NonCommercial License](https://creativecommons.org/licenses/by/4.0/), which permits use, distribution and reproduction in any medium, provided the original work is properly cited and is not used for commercial purposes.

Abstract The El Niño–Southern Oscillation (ENSO) strongly influences phytoplankton in the tropical Pacific, with El Niño conditions suppressing productivity in the equatorial Pacific (EP) and placing nutritional stresses on marine ecosystems. The Geophysical Fluid Dynamics Laboratory’s (GFDL) Earth System Model version 4.1 (ESM4.1) captures observed ENSO–chlorophyll patterns ($r = 0.57$) much better than GFDL’s previous ESM2M ($r = 0.23$). Most notably, the observed post-El Niño “chlorophyll rebound” is substantially improved in ESM4.1 ($r = 0.52$). We find that an anomalous increase in iron propagation from western Pacific (WP) subsurface to the cold tongue via the equatorial undercurrent (EUC) and subsequent post-El Niño surfacing, unresolved in ESM2M, is the primary driver of chlorophyll rebound. We also find that this chlorophyll rebound is augmented by high post-El Niño dust-iron deposition anomalies in the eastern EP. This post-El Niño chlorophyll rebound provides a previously unrecognized source of marine ecosystem resilience independent from the La Niña that sometimes follows.

Plain Language Summary In the tropical Pacific, year-to-year changes in chlorophyll, a proxy for the phytoplankton base of ocean food webs, is dominated by the El Niño–Southern Oscillation. El Niño, triggered by westerly wind anomalies and subsequent redistributions of upper ocean heat content, can sharply reduce the regional supply of nutrients limiting phytoplankton growth. A new Earth System Model captures not only the onset and extent of chlorophyll anomalies during El Niño events, but also a pronounced post-El Niño “chlorophyll rebound” that produces positive equatorial Pacific chlorophyll anomalies in the summer following El Niño events. This post-El Niño chlorophyll rebound is primarily driven by positive iron anomalies propagated from the subsurface western Pacific to the surface eastern Pacific cold tongue via the Equatorial Undercurrent. High post-El Niño dust deposition anomalies arising from dry land conditions in Central and South America augment the post-El Niño chlorophyll rebound. This post-El Niño chlorophyll rebound provides a key source of resilience to marine ecosystems in the equatorial Pacific.

1. Introduction

The ENSO profoundly impacts the physical and ecological conditions in the tropical Pacific (Barkley et al., 2018; Chatterjee et al., 2017; Lehodey et al., 2006; McClanahan et al., 2019; Salinas-de-León et al., 2020). The ocean color remote sensing detected extensive ENSO-associated variability in marine chlorophyll in the tropical Pacific (F. Chavez et al., 1999; McPhaden et al., 2006; Strutton et al., 2008; Park et al., 2011). F. Chavez et al. (1999) documented record low chlorophyll in the EP at the El Niño mature state in boreal winter 1997/1998 at about 0.05 $\mu\text{g/L}$, causing mass mortalities within marine ecosystems and severe disruptions of fisheries and coastal communities (F. P. Chavez and Messié, 2009). These lows in chlorophyll anomaly, however, were followed by a dramatic recovery, or “chlorophyll rebound,” that produced positive chlorophyll anomaly about 1 $\mu\text{g/L}$ (fivefold larger than climatology 0.2 $\mu\text{g/L}$) in 1998 boreal summer as decayed El Niño and transition to La Niña onset. These variations have been associated with the dynamic coupling to ENSO through the generation of equatorial Kelvin waves, modulating EUC and thermocline delivery of nutrients to the euphotic zone (Gierach et al., 2013; Gorgues et al., 2010; Radenac et al., 2012; Wilson & Coles, 2005).

Representation of iron limitation of phytoplankton growth is key to understand the low EP chlorophyll mean state under high macronutrient levels (F. Chavez et al., 1999; Landry et al., 1997; Le Borgne et al., 2002; Murray et al., 1992). Global earth system models (ESMs) with embedded marine biogeochemical models have

Supervision: John P. Dunne, Charles A. Stock
Writing – review & editing: Hyung-Gyu Lim, John P. Dunne, Charles A. Stock, Paul Ginoux, Jasmin G. John, John Krasting

successfully simulated the iron-limited mean state of the tropical Pacific (Aumont & Bopp, 2006; Aumont et al., 2015; Moore et al., 2013; Paulsen et al., 2017; Stock et al., 2020). Extensive ENSO analysis within physical climate models and subsequent refinements have yielded increasing skillful ENSO simulations (Capotondi et al., 2015; Planton et al., 2021), with the GFDL models evaluated herein providing robust simulations of ENSO teleconnections patterns, frequency, amplitude, and aspects of ENSO diversity (Dunne et al., 2012, 2020; Kug et al., 2010; Wittenberg et al., 2006). Extension of these efforts to ESMs has furthermore revealed skillful depictions of ENSO-driven chlorophyll evolution, including chlorophyll feedbacks on ocean temperature and climate (Anderson et al., 2009; Park et al., 2014b, 2018). Less attention, however, has been paid to post-El Niño chlorophyll rebound, with studies suggesting under-representation in ESMs (Park et al., 2018).

These studies also omit the potential influence of dynamic variations in the delivery of iron dust to the EP (Duce & Tindale, 1991; Landry et al., 1997). El Niño events are associated with dry conditions over land areas surrounding the EP with well documented responses in dust and fire activity (Evans et al., 2016; Le Page et al., 2008; McPhaden et al., 2006; Woodward et al., 2008). The ENSO driven dust-iron anomalies augments internal ocean ENSO-chlorophyll patterns in GFDL ESM4.1 (Dunne et al., 2020) with its parameterization for dynamic-dust-related iron deposition (Evans et al., 2016; Horowitz et al., 2020; Stock et al., 2020), unresolved in previous generation GFDL ESM2M (Dunne et al., 2013).

In this study, we explore the pattern correlation of ENSO-driven chlorophyll anomalies and representation of the post El-Niño chlorophyll rebound in ESM2M and ESM4.1. We then diagnose oceanic and atmospheric drivers underlying the post El-Niño chlorophyll rebound, taking advantage of ESM4.1's inclusion of dynamic feedbacks between climate conditions, dust emissions, and dust-iron deposition.

2. Data and Methods

We analyzed preindustrial control (piControl) simulations from two generations of GFDL earth system models: years 1001–1100 of ESM2M (Dunne et al., 2012, 2013) which participated in the Coupled Model Intercomparison Project Phase 5 (CMIP5) (Taylor et al., 2012); and years 501–645 of ESM4.1 (Dunne et al., 2020; Stock et al., 2020) which participated in CMIP6 (Eyring et al., 2016). The Major advances in ESM4.1 relative to ESM2M are described in Text S1 in Supporting Information S1.

To quantify the role of dynamically varying dust deposition in the post-El Niño chlorophyll rebound, we conducted an additional ESM4.1 piControl simulation (ESM4.1-static), where the dynamically varying dust and iron delivery to the ocean was replaced by a monthly climatology at each model grid cell derived from years 501–645 of the ESM4.1 piControl.

Satellite-derived ocean color was obtained from the European Space Agency Ocean Colour Climate Change Initiative project (ESA-CCI) version 4.2 (Sathyendranath et al., 2020) for use in estimating observed ENSO-associated surface chlorophyll concentration. Sea surface temperature (SST) data was obtained from the NOAA Extended Reconstructed SST version 5 (ERSST v5) (Huang et al., 2017). Vertical temperature profiles were obtained from version 3.4.2 of the Simple Ocean Data Assimilation (SODA) (Carton et al., 2018). Two satellite-derived aerosol optical thicknesses were obtained from the NOAA Climate Data Record (CDR) of AVHRR Daily and Monthly Aerosol Optical Thickness (AOT) over Global Oceans, Version 3.0 (Zhao & NOAA-CDR-Program, 2017) and SeaWiFS Deep Blue Level 3 monthly product which contains monthly global gridded ($1^\circ \times 1^\circ$) data derived from SeaWiFS Deep Blue Level 3 daily gridded data (Hsu et al., 2013). All data sets were converted to 1° horizontal resolution and analyzed over September 1997 until December 2018. AOTs were available from AVHRR from January 2002 to December 2018 and SeaWiFS from September 1997 to December 2007. Linear trends and seasonal cycles were removed from all data sets. All data sets are smoothed using a 3-month running mean to focus on the seasonal ENSO-chlorophyll evolution and its variability. The November to January (NDJ) averaged SST anomalies (SSTa) in the Niño3.4 region (170° – 120° W, 5° N– 5° S; Niño3.4 SSTa) (Trenberth, 1997) was employed to diagnose general ENSO influences. Further methods of regression and correlation analysis of NDJ Niño3.4 SSTa, so called ENSO regression or correlation, are described in Text S2 in Supporting Information S1.

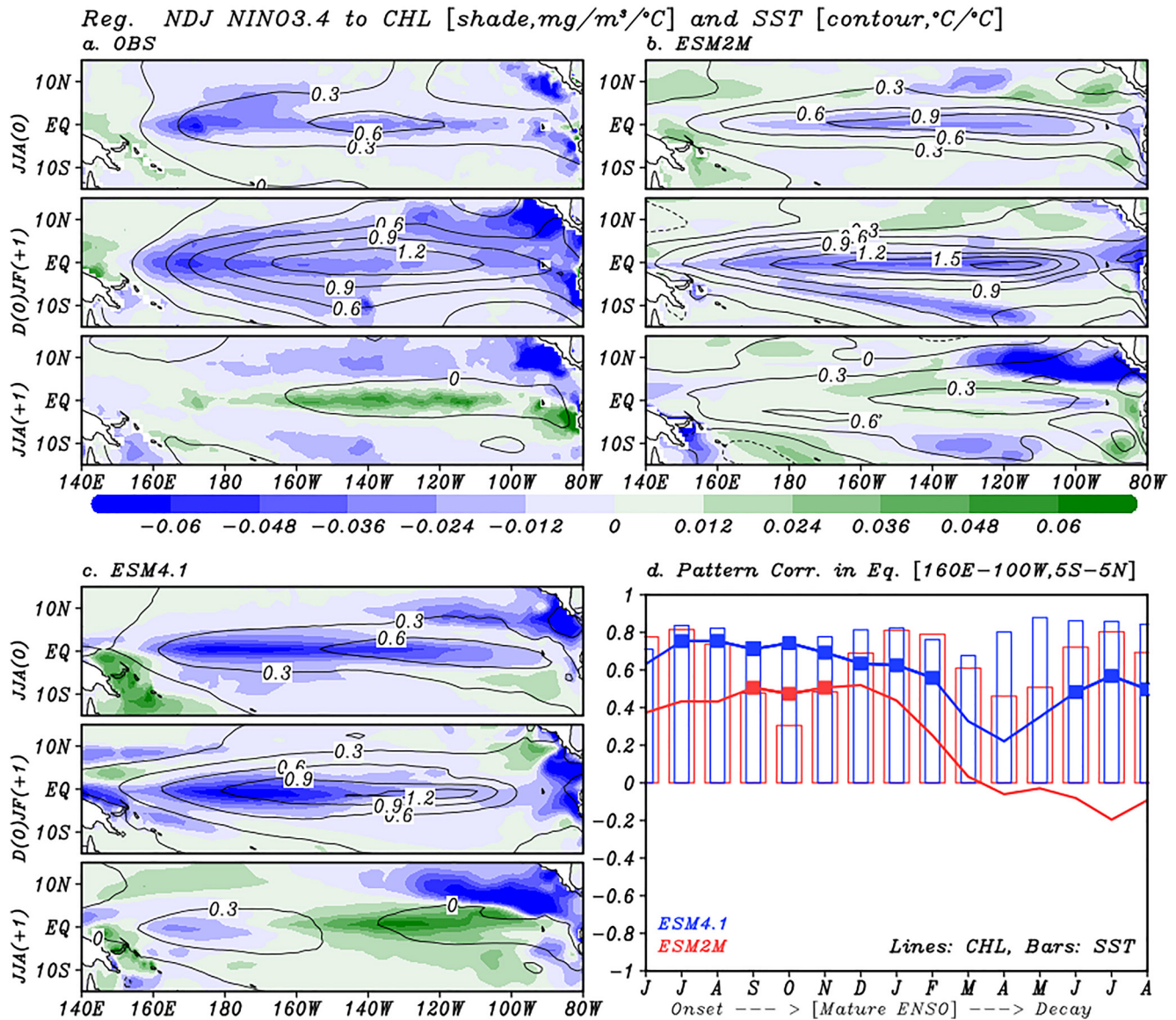


Figure 1. Spatially resolved ENSO-regression of temperature (contours, °C/°C) and chlorophyll concentration (shading, mg/m³/°C) anomalies against ENSO in (a) satellite, SODA, (b) ESM2M, and (c) ESM4.1. Values are shown for ENSO onset (JJA[0]), mature state (D[0]JF[+1]), and decay (JJA[+1]) ENSO states; (d) pattern correlations of ESM2M (red) and ESM4.1 (blue) regression coefficients (i.e., panels b and c) with SODA (bars) and satellite chlorophyll (lines; square symbols denote the Student's *t*-test statistical significance at 95% confidence level) regression coefficients (i.e., panel a) in the EP (160°E–100°W, 5°N–5°S).

3. Results

3.1. ENSO Driven Chlorophyll Evolution

The evolution of ENSO-regressed SSTa is shown in Figure 1 (contour) for ERSST, ESM2M, and ESM4.1. ENSO-regressed SSTa is shown for the ENSO onset during the boreal summer (June to August; JJA[0]), the mature ENSO state in boreal winter (December to February; D[0]JF[+1]), and the decaying ENSO state during the next boreal summer (June to August; JJA[+1]). While ESM2M exaggerates ENSO-regressed SSTa patterns across all three phases, ESM4.1 simulates better SSTa pattern evolutions (Figures 1a–1c; contour). While the observed pattern correlations of ENSO SSTa evolution in EP (160°E–100°W, 5°N–5°S) with ESM2M are ranged from 0.31 to 0.81 from onset to decay with an overall mean 0.65, that with ESM4.1 are ranged 0.68 to 0.87 with an overall mean 0.8 (Figure 1d; bars).

The evolution of ENSO-regressed surface chlorophyll anomaly in satellite-based observations is also better captured in ESM4.1 than ESM2M (Figures 1a–1c; shading). The pattern correlations of ENSO-chlorophyll from onset to decay simulated in ESM2M achieve the range of -0.19 to 0.52 with an overall mean of 0.23 , while ESM4.1 achieves the range of 0.22 to 0.75 with an overall mean 0.57 (Figure 1d, lines). Most critically, ESM4.1 accurately simulates the post-El Niño chlorophyll rebound 6 months after the mature ENSO state (Figure 1c, JJA[+1]; Figure 1d, blue line [$r = 0.52$]), which is not captured in ESM2M (Figure 1b, JJA[+1]; Figure 1d, red line [$r = -0.12$]). It is noteworthy that the lack of rebound in ESM2M is associated with post-El Niño warm SSTa in JJA(+1) in the eastern EP in accordance with stronger amplitude and longer persistency of ENSO in ESM2M than observation. This warm SSTa in JJA(+1) in ESM2M could linger on the nutrient supply to the euphotic zone (Park, Kug, & Park, 2014). The warm SSTa in JJA(+1) in ESM4.1, in contrast, have largely subsided in the eastern EP.

ENSO-regressed surface dissolved iron anomalies reveal that both ESM2M and ESM4.1 exhibit reductions in surface iron during the onset and mature phase of El Niño. This is consistent with westerly wind anomalies generating a downwelling Kelvin wave that deepens the thermocline in the eastern EP, suppressing the supply of subsurface iron (F. Chavez et al., 1999). While regression values are maximized at approximately $6 \text{ nmole/m}^3/\text{C}$, simulated iron concentrations are still limited within $10\text{--}100 \text{ nmole/m}^3$ in the equatorial Pacific (Stock et al., 2020). During the El Niño decay phase, ESM4.1 exhibits a marked positive iron anomaly in the eastern EP (Figure 2b) that is not captured in ESM2M (Figure 2a). This positive iron anomaly coincides with the chlorophyll rebound in ESM4.1, consistent with report from F. Chavez et al. (1999). The contrast between ESM2M and ESM4.1 is also apparent in the lead-lag relationship between iron anomalies averaged in the eastern EP ($160^\circ\text{--}100^\circ\text{W}$, $5^\circ\text{S}\text{--}5^\circ\text{N}$) and NDJ Niño3.4 SSTa (Figure 2c). The eastern EP iron anomalies and NDJ Niño3.4 SSTa are positively correlated in El Niño decay phase in ESM4.1, $r = 0.62$.

In contrast to iron, analogous regressions against surface nitrate do not show strong contrast between ESM2M and ESM4.1 (Figure S1 in Supporting Information S1). Both models generate negative nitrate anomalies throughout the El Niño onset and maturation, turning weakening negative anomalies due to weakening SSTa at El Niño decay. Since nitrate is not the limiting nutrient controlling the EP chlorophyll mean state in ESM4.1 (Stock et al., 2020), patterns of rather positive iron anomalies against the weakening SSTa and nitrate anomalies in post-El Niño is a key role in controlling the post-El Niño chlorophyll rebound.

3.2. An Oceanic Rebound Pathway: Iron Propagation Through the EUC

To assess oceanic mechanism underlying the post-El Niño chlorophyll rebound, the NDJ Niño3.4 SSTa regression analysis is employed to determine influences of ENSO onset to decay states in vertical structures of temperature and iron anomalies averaged in the EP ($2^\circ\text{S}\text{--}2^\circ\text{N}$; Figure 3). As before, we use the NDJ index because this allows us to assess the relationship with the fully developed ENSO state (see Section 2). Warm temperature anomalies in the EP are apparent in both ESM simulations and SODA during the El Niño onset and mature state (Figures 3a–3c), reflecting the downwelling Kelvin wave propagating from west to east and deepening thermocline (Timmermann et al., 2018). This warming signal lingers on the eastern EP surface and subsurface during the El Niño decay in ESM2M (Figure 3a). In contrast, ESM4.1 simulates cooler surface and subsurface waters in the eastern EP, agreeing much better with SODA (Figures 3b and 3c).

Dissolved iron anomalies along the transect exhibit a strong inverse relationship with temperature anomalies, similar contrasts among ESM2M and ESM4.1 (Figures 3d and 3e). That is, onset and mature ENSO states in both ESM2M and ESM4.1 exhibit prominent negative iron anomalies in anomalous warm waters in the top 200 m, and positive anomalies in cold subsurface anomalies that propagate from west to east from El Niño onset to decay.

Lead-lag relationship of correlation coefficients between monthly Niño3.4 SSTa and monthly iron anomalies in the WP subsurface region ($130^\circ\text{--}160^\circ\text{E}$, $2^\circ\text{N}\text{--}2^\circ\text{S}$, $100\text{--}200 \text{ m}$ depth) show that both ESM2M and ESM4.1 generate anomalously high subsurface iron concentration in WP throughout El Niño events (Figure S2 in Supporting Information S1). Anomalous cold-water formation in the WP subsurface is not only a necessary precondition for the well documented occurrence of La Niña following El Niño events (Jin, 1997; Wittenberg et al., 2006; Wyrski, 1985) but is also a key to trapping iron in the WP subsurface. Peaks of iron anomalies trapped in the WP subsurface are similarly represented in boreal autumn from September to November (SON[0]), 3-month before the mature ENSO states in both ESM2M ($r = 0.77$) and ESM4.1 ($r = 0.78$).

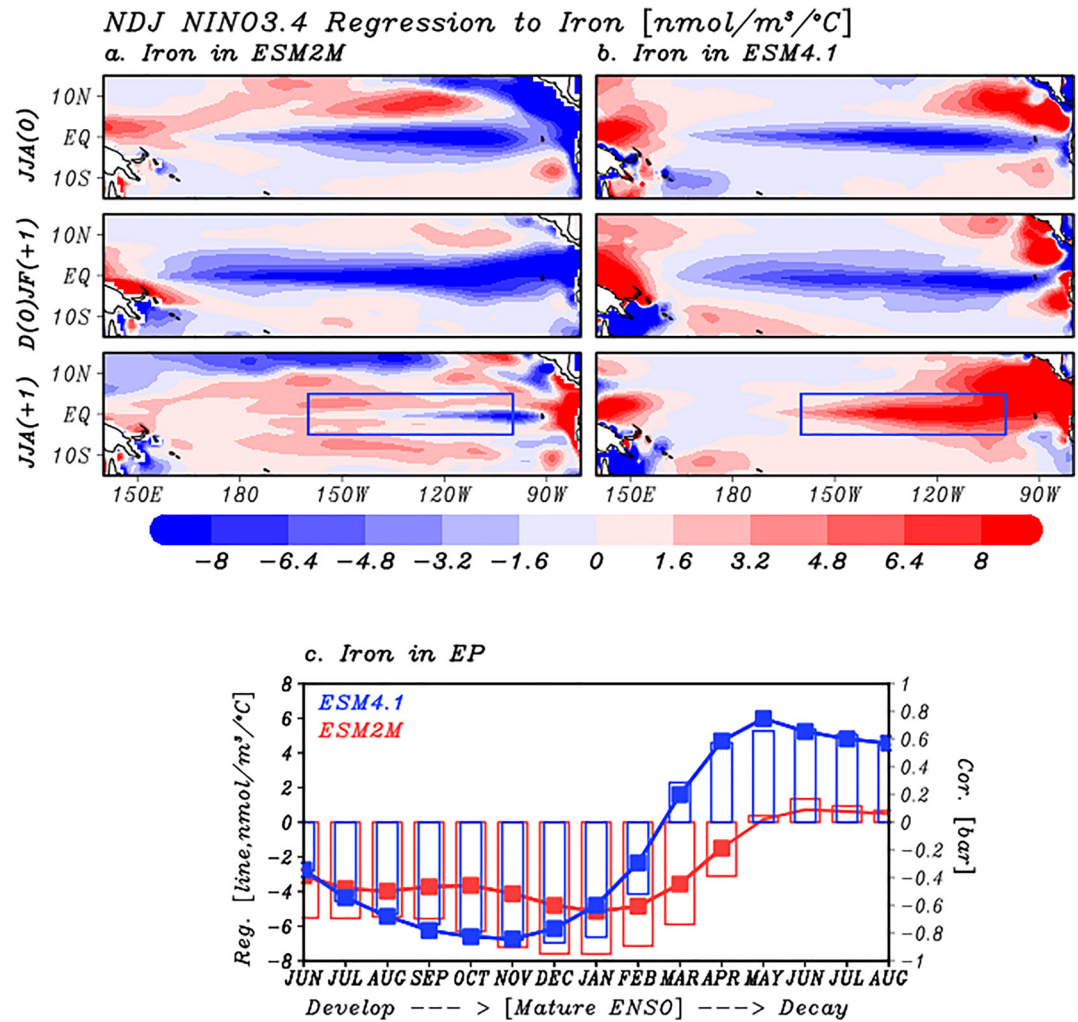


Figure 2. ENSO-regressed patterns in spatially resolved surface iron concentration anomalies (nmol/m³/°C) in (a) ESM2M and (b) ESM4.1. (c) lead-lag ENSO regression (lines; square symbols denote the Student's *t*-test statistical significance at 95% confidence level) and correlation (bar) coefficients in regional monthly iron concentration anomalies in the eastern EP (160°–100°W, 5°S–5°N).

These ENSO-related positive iron anomalies in the WP subsurface can propagate to the eastern EP surface following the thermocline and easterly oceanic current of EUC. The iron propagation in ESM2M, however, remains below 50 m in the eastern EP (Figure 3d), mirroring the temperature patterns (Figure 3a) and failing to impact the surface iron (Figure 2). Instead, strong negative iron anomalies associated with lingering warm temperature anomalies in the EP subsurface continue to upwell to the surface. The positive iron anomalies in the WP subsurface in ESM4.1, in contrast, propagate to the eastern EP surface (Figure 3e) in a manner consistent with the eastward propagation of cold ocean temperature anomalies (Figures 3b and 3c).

To further illustrate the relationship between the eastward propagation of iron anomalies in the EUC and the post-El Niño chlorophyll rebound, the lead-lag relationship between monthly WP subsurface iron anomalies at SON(0) and both surface chlorophyll and iron anomalies in the eastern EP (160°–100°W, 5°N–5°S) are shown in Figures 3f and S3 in Supporting Information S1. The iron anomalies in the WP subsurface at SON(0) are significantly associated with iron and chlorophyll anomalies in the eastern EP 9-month later in ESM4.1, while minimal responses are apparent in ESM2M.

The strength of these relationships in ESM4.1, together with its mechanistic underpinnings and the absence of the post-El Niño chlorophyll rebound in the model lacking this mechanism, suggests that the oceanic role in the eastward propagation of WP subsurface iron anomalies in the EUC and subsequent surfacing iron anomalies in

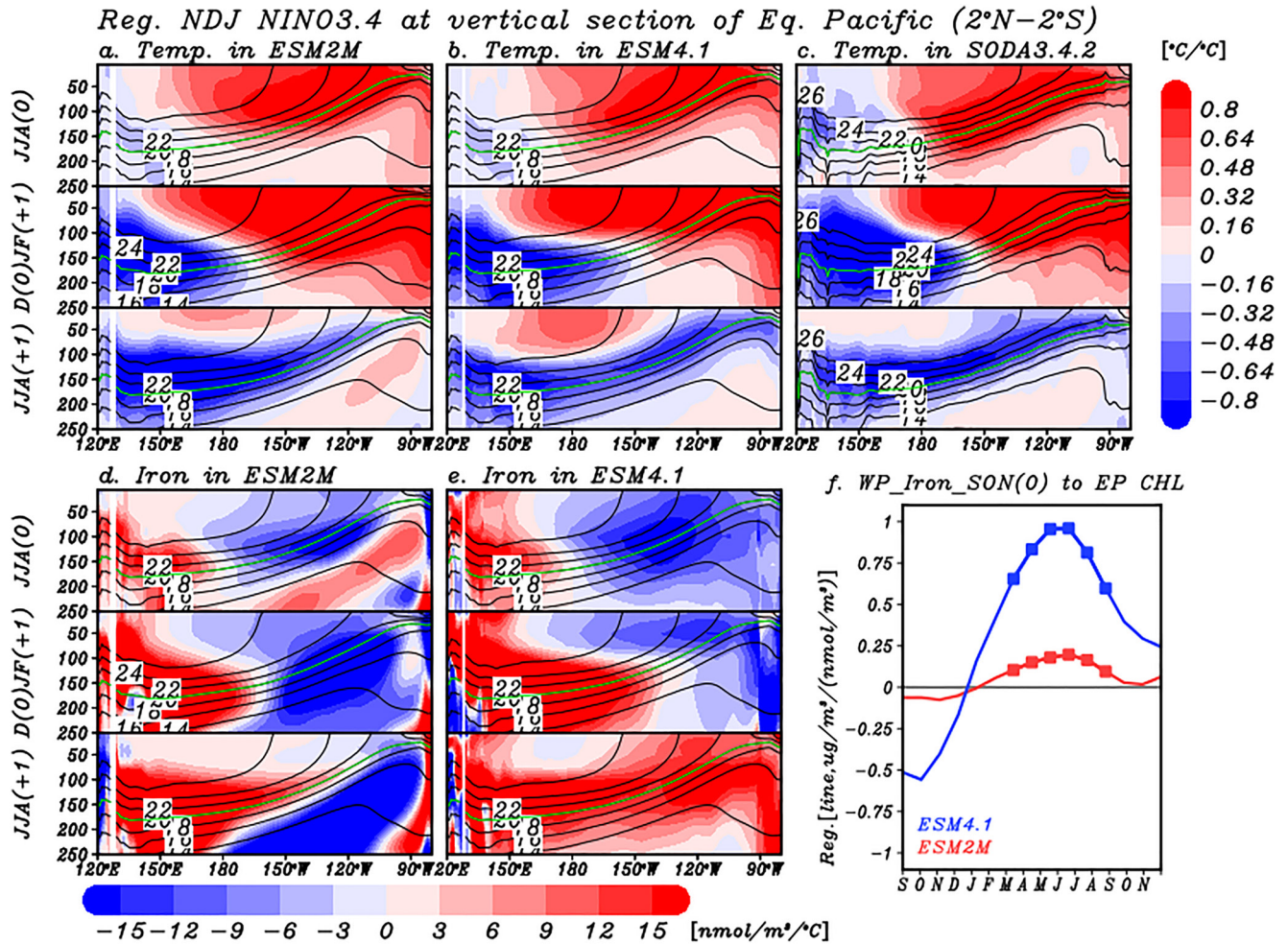


Figure 3. ENSO-regressed coefficients of vertical sections of equatorial temperature anomalies in (a) ESM2M, (b) ESM4.1, (c) SODA and dissolved iron concentration anomalies (shading) in (d) ESM2M, (e) ESM4.1. The temperature climatology from each model and SODA has been overlaid (contours) to aid interpretation and 20°C isotherm (green line) at equator (2°N–2°S). (f) Regressed coefficients (square symbols denote the statistical significance at 95% confidence level) of iron concentration anomalies in the WP subsurface region averaged in (130°–160°E, 2°N–2°S, 100–200 m depth) at SON(0) against the eastern EP surface (160°–100°W, 5°S–5°N) monthly chlorophyll concentration anomalies simulated in ESM2M (red) and ESM4.1 (blue).

the shoaling thermocline of the EP surface is likely a primary driver of the post-El Niño chlorophyll rebound. We note that a chlorophyll rebound would likely occur with adequate thermocline shoaling even without the eastward propagation of WP iron anomalies (as long as iron concentrations increase with depth below the euphotic zone). However, our results emphasize an important connection between the iron characteristics of the WP subsurface waters and fueling the EP rebound.

3.3. An Atmospheric Rebound Pathway: ENSO Driven Iron Deposition

The previous section attributed oceanic iron responses to ENSO and its propagating patterns into the eastern EP through the EUC in ESM4.1. While this mechanism accounts for the iron propagation via the interior ocean, we can also evaluate another potential driving mechanism for the chlorophyll rebound in ESM4.1: the atmospheric dust-iron response to ENSO (Dunne et al., 2020; Evans et al., 2016; Stock et al., 2020).

The ENSO-regressed atmospheric iron deposition anomalies on the surface in the eastern EP in ESM4.1 are shown in Figure 4a. ESM4.1 simulates increases in iron depositions exceeding 0.34 $\mu\text{mol}/\text{m}^2/\text{yr}/^\circ\text{C}$ during all ENSO stages. The amplitude is highest, 0.89 $\mu\text{mol}/\text{m}^2/\text{yr}/^\circ\text{C}$, in boreal spring (from March to May) when climatological dust emission is commonly high (Horowitz et al., 2020). Despite the lack of observed iron dust flux timeseries, we compare timeseries in aerosol optical thickness (AOT) anomalies obtained from AVHRR and

NDJ NINO3.4 Reg. Dynamic dust effect (ESM4.1 - ESM4.1-static)

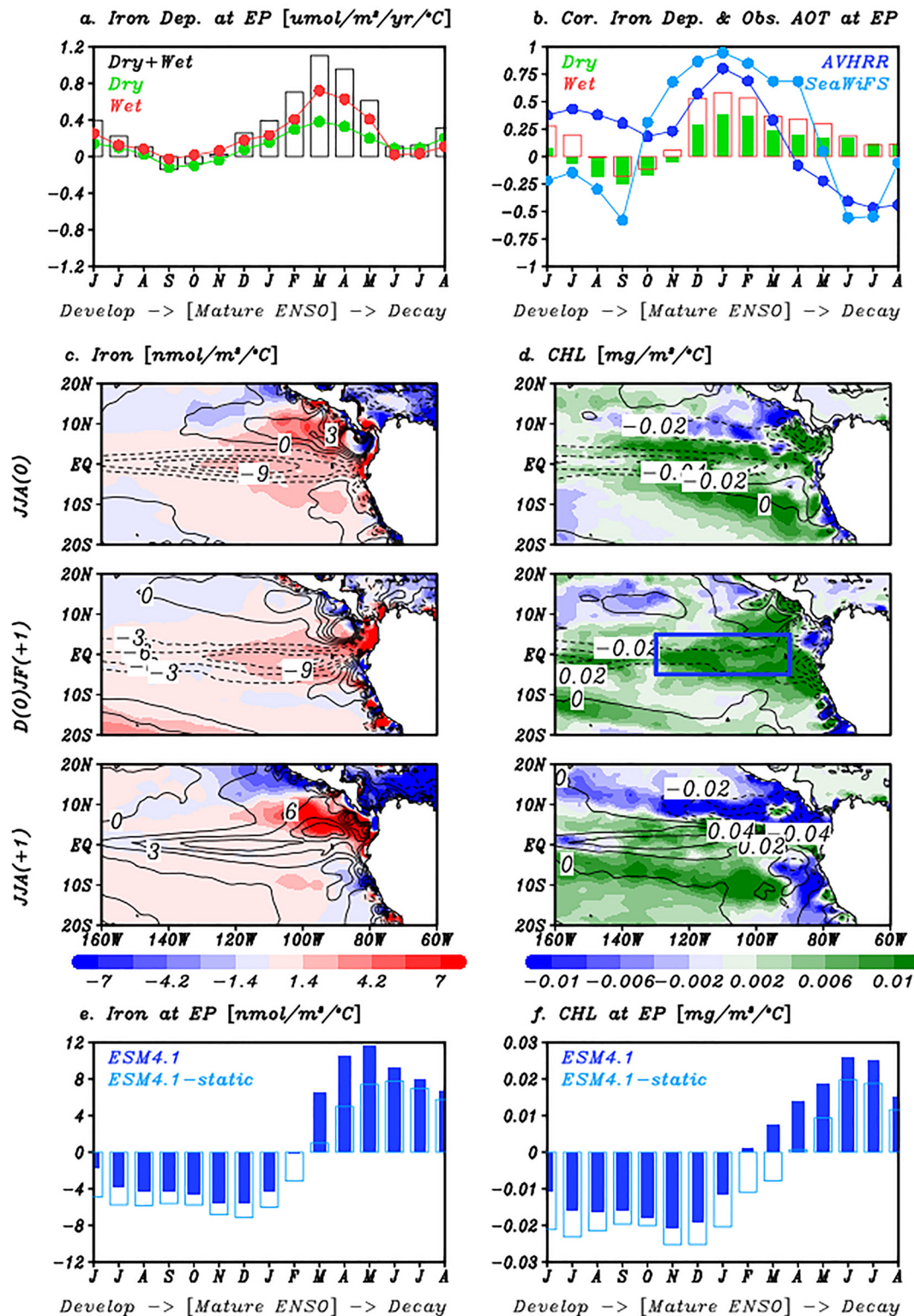


Figure 4.

SeaWiFS data sets associated with ENSO. AOT anomalies are positively correlated with ENSO in the eastern EP throughout winter and spring seasons ($r = 0.35\text{--}0.68$) that provide iron deposition increases simulated in ESM4.1 (Figures 4a and 4b).

To investigate the dynamic dust effect on the post-El Niño chlorophyll rebound, we compare ESM4.1 with an otherwise identically forced simulation that replaces dynamic dust and iron deposition to the ocean with monthly climatological forcing obtained from ESM4.1 (ESM4.1-static, Section 2). Therefore, the long-term mean of iron depositions in ESM4.1-static is the same as in ESM4.1 but is not varying interannually.

The difference of ENSO-iron and chlorophyll sensitivities between ESM4.1 and ESM4.1-static simulations (Figures 4c and 4d) is used to represent the imprint of dynamic dust effect. The core patterns of the post-El Niño iron and chlorophyll rebounds are also present in ESM4.1-static (Figures 4c and 4d; contour), implying that the oceanic pathway is the major driver to simulating the post-El Niño chlorophyll rebound. However, the increased dust-iron deposition anomalies associated with ENSO in ESM4.1 generally enhance positive iron and chlorophyll anomalies across all ENSO stages in the eastern tropical Pacific (Figures 4c and 4d). The high dust-iron response is largest near 10°N where values in aerosol optical depth (Choobari et al., 2014) and iron deposition (Duce & Tindale, 1991) are also high.

To further quantify the dynamic dust-iron effect, ENSO-regressed iron and chlorophyll anomalies averaged in the eastern EP in ESM4.1 and ESM4.1-static are shown in Figures 4e and 4f. The dynamic dust in ESM4.1 modulates the sensitivity of ENSO-regressed iron anomalies, but the amplitude of its sensitivity is seasonally dependent. That is, dynamic dust suppressed the iron sensitivity in onset and mature ENSO states relative to the static dust case, but enhanced iron sensitivity in decaying ENSO state. ESM4.1 exhibits lower amplitude of negative iron anomalies in onset and mature ENSO (-46.8%) due to high dust-iron deposition relative to ESM4.1-static ($-3.86\text{ nmol/m}^3/^{\circ}\text{C}$ in ESM4.1; $-5.66\text{ nmol/m}^3/^{\circ}\text{C}$ in ESM4.1-static). The amplitude of positive iron anomalies in the decaying ENSO state is higher in ESM4.1 than in ESM4.1-static by 36.1% because both the oceanic and atmospheric iron transport effects are reflected in ESM4.1 ($8.83\text{ nmol/m}^3/^{\circ}\text{C}$ in ESM4.1; $5.64\text{ nmol/m}^3/^{\circ}\text{C}$ in ESM4.1-static).

The dynamic dust related iron sensitivity against ENSO events propagates to the ENSO-chlorophyll responses. The amplitude of negative chlorophyll anomalies in onset and mature ENSO states is weaker in ESM4.1 about 46.1% than ESM4.1-static ($-0.014\text{ mg/m}^3/^{\circ}\text{C}$ in ESM4.1; $-0.021\text{ mg/m}^3/^{\circ}\text{C}$ in ESM4.1-static). The amplitude of positive chlorophyll responses in the decaying ENSO state is stronger in ESM4.1 than ESM4.1-static about 51% ($0.018\text{ mg/m}^3/^{\circ}\text{C}$ in ESM4.1; $0.009\text{ mg/m}^3/^{\circ}\text{C}$ in ESM4.1-static).

4. Summary and Discussion

Strong interannual variability in marine chlorophyll in the tropical Pacific has been reported in connection with ENSO in both observations (F. Chavez et al., 1999; Park et al., 2011; Strutton et al., 2008) and models (Lee et al., 2014; Park et al., 2018; Zhang et al., 2018). The present study builds on past work by describing how ESM4.1 captures the observed patterns in ENSO driven chlorophyll anomalies compared to the previous generation ESM2M. With the benefit of an improved ESM4.1, we find that the ENSO simulation in ESM2M is too strong. This limits the post-El Niño iron resupply in the eastern EP and suppresses the post-El Niño chlorophyll rebound. This unrealistic simulation in ESM2M has been relatively tempered in ESM4.1 via the better performance in simulating ENSO events (Dunne et al., 2020; Planton et al., 2021).

In addition, we show that both ESM2M and ESM4.1 exhibit iron trapping during ENSO in the WP subsurface region. ESM4.1 simulates the trapped iron anomaly propagated to the eastern EP surface. The unresolved iron transport and post-El Niño chlorophyll rebound patterns in ESM2M are hampered by the remained warming signal in the eastern EP surface. The simulation of post-El Niño chlorophyll rebound has previously only been adequately captured after targeted adjustments to the underlying model via ideally reduced grazing pressure in zooplankton or imposed additional iron (Gorgues et al., 2010; Tian et al., 2021). These interactions are now

Figure 4. (a) ENSO-regression coefficient of dry (green), wet (red), and total (black bar) iron deposition ($\mu\text{mol/m}^2/\text{yr}/^{\circ}\text{C}$) in ESM4.1 averaged in the eastern EP ($160^{\circ}\text{--}100^{\circ}\text{W}$, $5^{\circ}\text{S}\text{--}5^{\circ}\text{N}$). Panel (b) is the same as (a) but for correlation coefficients in dry (green bar) and wet (red bar) deposition anomalies in ESM4.1 and observed aerosol optical thicknesses (AOT) obtained from AVHRR (blue line) and SeaWiFS (sky blue line). Spatially resolved ENSO-regression coefficient differences (dynamic dust effects; shading) of (c) iron and (d) chlorophyll anomalies between ESM4.1 and ESM4.1-static; contours denote the ENSO-regression coefficient in iron and chlorophyll anomalies in ESM4.1-static. ENSO-regressed (e) iron and (f) chlorophyll anomalies averaged in the eastern EP in ESM4.1 (blue) and ESM4.1-static (sky blue).

captured in ESM4.1 by physical improvements of ENSO simulation (Planton et al., 2021), achieved from reasonable vertical ocean temperature profile in hybrid vertical coordinate, increased oceanic horizontal resolution, better fidelity in rainfall, zonal windstress, and net heatflux responses against ENSO (Adcroft et al., 2019; Dunne et al., 2020; Zhao et al., 2018) and potentially affected by the enhanced coupling between phytoplankton and zooplankton food web dynamics (Stock et al., 2014, 2020).

The analysis herein focused on understanding the predominant chlorophyll rebound behavior as reflected in ENSO events. ENSO events, however, can exhibit diverse characteristics (Kug et al., 2009; Stuecker et al., 2013; Timmermann et al., 2018; Yeh et al., 2009) and include inter-basin interactions with other climate modes (Cai et al., 2019; Ham et al., 2013; Le et al., 2020; Ohba & Ueda, 2007; Yoo et al., 2020). Increasingly skillful representation of the “ENSO diversity” in climate and earth systems models (Capotondi et al., 2015; Gierach et al., 2012; Lee et al., 2014; Planton et al., 2021; Racault et al., 2017; Tian et al., 2021) is creating the potential to analyze the sensitivity of the post-El Niño chlorophyll rebound to this diversity.

The ENSO-related dissolved iron response plays a critical role in ecosystem variability in the tropical Pacific. To achieve realistic simulation in iron-cycle variability, allochthonous iron fluxes from land vegetation to dust onto the ocean surface are parameterized in ESM4.1 (Dunne et al., 2020; Evans et al., 2016; Stock et al., 2020). While general patterns of ENSO-chlorophyll anomalies were primarily controlled by ocean circulation, dynamic dust alters seasonal amplitude of ENSO-chlorophyll, suppressing anomalies in the onset and mature ENSO states and enhancing anomalies in the decaying ENSO state. Therefore, the dynamic dust plays a role in determining the amplitude, timing, and of marine ecosystem variability in the EP. The suggested modeling approach may be applied to other ESMs, though sensitivity might differ for other dust-iron parameterizations. One such mechanism captured in ESM4.1 is the role of climate and resulting dust emissions and transport variabilities so further changes in hydrological cycles, land vegetations, and dust emissions (Adler et al., 2017; Horowitz et al., 2020; Shao et al., 2013; Shiogama et al., 2022) may alter future changes in the marine ecosystem.

Our analysis with ESM4.1 provides new insight in revisiting the well-known phenomena of ENSO-chlorophyll covariances with better mechanistic representation of physical-biological interaction from the anomalous iron propagation. In addition, the new parameterization of dynamic dust-iron in ESM4.1 allows us to expand the potential for attribution into dust-climate-biological interaction which have rich interplay especially in the tropical Pacific where the iron is limited for marine ecosystem. Most importantly, these results with ESM4.1 demonstrate that models can capture the observed delayed response of ENSO “post-El Niño chlorophyll rebound” and provides the promising new source of marine ecosystem predictability in the climate system.

Data Availability Statement

Ocean color chlorophyll, ESA-CCI-4.2, is available online <https://climate.esa.int/en/projects/ocean-colour/> and model results are available for community analysis via the Earth System Grid Federation (<https://esgf-node.llnl.gov/projects/esgf-llnl/>) and GFDL's public data server (<https://data1.gfdl.noaa.gov/>; Krasting et al., 2018). The GFDL ESM2M, ESM4.1, ESM4.1-static simulation data used for ENSO related chlorophyll and iron analysis in the study are available at <https://doi.org/10.5281/zenodo.5525089>.

References

- Adcroft, A., Anderson, W., Balaji, V., Blanton, C., Bushuk, M., Dufour, C. O., et al. (2019). The GFDL Global Ocean and sea Ice model OM4.0: Model description and simulation features. *Journal of Advances in Modeling Earth Systems*, 11(10), 3167–3211. <https://doi.org/10.1029/2019ms001726>
- Adler, R. F., Gu, G., Sapiano, M., Wang, J.-J., & Huffman, G. J. (2017). Global precipitation: Means, variations and trends during the satellite era (1979–2014). *Surveys in Geophysics*, 38(4), 679–699. <https://doi.org/10.1007/s10712-017-9416-4>
- Anderson, W., Gnanadesikan, A., & Wittenberg, A. (2009). Regional impacts of ocean color on tropical Pacific variability. *Ocean Science*, 5(3), 313. <https://doi.org/10.5194/os-5-313-2009>
- Aumont, O., & Bopp, L. (2006). Globalizing results from ocean in situ iron fertilization studies. *Global Biogeochemical Cycles*, 20(2). <https://doi.org/10.1029/2005gb002591>
- Aumont, O., Ethé, C., Tagliabue, A., Bopp, L., & Gehlen, M. (2015). PISCES-v2: An ocean biogeochemical model for carbon and ecosystem studies. *Geoscientific Model Development*, 8(8), 2465–2513. <https://doi.org/10.5194/gmd-8-2465-2015>
- Barkley, H. C., Cohen, A. L., Mollica, N. R., Brainard, R. E., Rivera, H. E., DeCarlo, T. M., et al. (2018). Repeat bleaching of a central Pacific coral reef over the past six decades (1960–2016). *Communications Biology*, 1(1), 177. <https://doi.org/10.1038/s42003-018-0183-7>
- Cai, W., Wu, L., Lengaigne, M., Li, T., McGregor, S., Kug, J.-S., et al. (2019). Pan-tropical climate interactions. *Science*, 363(6430), eaav4236.

Acknowledgments

The authors thank Cristina Schultz (Princeton University AOS/GFDL-NOAA) and Elizabeth J. Drenkard (NOAA-GFDL) for providing earlier reviews of our results and appreciate valuable comments for elevating the quality of the manuscript from two anonymous reviewers. The authors thank Aparna Radhakrishnan (Princeton University AOS/Cooperative Institute for Climate Science) and Hans Vahlenkamp (UCAR/NOAA-GFDL) for assisting the GFDL simulation data set hosting to public. H.-G. Lim is supported under award NA18OAR4320123 from the National Oceanic and Atmospheric Administration, U.S. Department of Commerce. The statements, findings, conclusions, and recommendations are those of the author(s) and do not necessarily reflect the views of the National Oceanic and Atmospheric Administration, or the U.S. Department of Commerce.

- Capotondi, A., Wittenberg, A. T., Newman, M., Di Lorenzo, E., Yu, J.-Y., Braconnot, P., et al. (2015). Understanding ENSO diversity. *Bulletin of the American Meteorological Society*, *96*(6), 921–938. <https://doi.org/10.1175/bams-d-13-00117.1>
- Carton, J. A., Chepurin, G. A., & Chen, L. (2018). SODA3: A new ocean climate reanalysis. *Journal of Climate*, *31*(17), 6967–6983. <https://doi.org/10.1175/jcli-d-18-0149.1>
- Chatterjee, A., Gierach, M. M., Sutton, A. J., Feely, R. A., Crisp, D., Elderling, A., et al. (2017). Influence of El Niño on atmospheric CO₂ over the tropical Pacific ocean: Findings from NASA's OCO-2 mission. *Science*, *358*(6360). <https://doi.org/10.1126/science.aam5776>
- Chavez, F., Strutton, P., Friederich, G., Feely, R., Feldman, G., Foley, D., & McPhaden, M. (1999). Biological and chemical response of the equatorial Pacific ocean to the 1997–98 El Niño. *Science*, *286*(5447), 2126–2131. <https://doi.org/10.1126/science.286.5447.2126>
- Chavez, F. P., & Messié, M. (2009). A comparison of eastern boundary upwelling ecosystems. *Progress in Oceanography*, *83*(1), 80–96. <https://doi.org/10.1016/j.pocean.2009.07.032>
- Choobari, O. A., Zawar-Reza, P., & Sturman, A. (2014). The global distribution of mineral dust and its impacts on the climate system: A review. *Atmospheric Research*, *138*, 152–165. <https://doi.org/10.1016/j.atmosres.2013.11.007>
- Duce, R. A., & Tindale, N. W. (1991). Atmospheric transport of iron and its deposition in the ocean. *Limnology & Oceanography*, *36*(8), 1715–1726. <https://doi.org/10.4319/lo.1991.36.8.1715>
- Dunne, J. P., Horowitz, L. W., Adcroft, A. J., Ginoux, P., Held, I. M., John, J. G., et al. (2020). The GFDL earth system model version 4.1 (GFDL-ESM 4.1): Overall coupled model description and simulation characteristics. *Journal of Advances in Modeling Earth Systems*, *12*(11), e2019MS002015. <https://doi.org/10.1029/2019ms002015>
- Dunne, J. P., John, J. G., Adcroft, A. J., Griffies, S. M., Hallberg, R. W., Shevliakova, E., et al. (2012). GFDL's ESM2 global coupled climate-carbon earth system models. Part I: Physical formulation and baseline simulation characteristics. *Journal of Climate*, *25*(19), 6646–6665. <https://doi.org/10.1175/jcli-d-11-00560.1>
- Dunne, J. P., John, J. G., Shevliakova, E., Stouffer, R. J., Krasting, J. P., Malyshev, S. L., et al. (2013). GFDL's ESM2 global coupled climate-carbon earth system models. Part II: Carbon system formulation and baseline simulation characteristics. *Journal of Climate*, *26*(7), 2247–2267. <https://doi.org/10.1175/jcli-d-12-00150.1>
- Evans, S., Ginoux, P., Malyshev, S., & Shevliakova, E. (2016). Climate-vegetation interaction and amplification of Australian dust variability. *Geophysical Research Letters*, *43*(22), 11–823. <https://doi.org/10.1002/2016gl071016>
- Eyring, V., Bony, S., Meehl, G. A., Senior, C. A., Stevens, B., Stouffer, R. J., & Taylor, K. E. (2016). Overview of the coupled model Intercomparison project phase 6 (CMIP6) experimental design and organization. *Geoscientific Model Development*, *9*(5), 1937–1958. <https://doi.org/10.5194/gmd-9-1937-2016>
- Gierach, M. M., Lee, T., Turk, D., & McPhaden, M. J. (2012). Biological response to the 1997–98 and 2009–10 El Niño events in the equatorial Pacific ocean. *Geophysical Research Letters*, *39*(10). <https://doi.org/10.1029/2012gl051103>
- Gierach, M. M., Messié, M., Lee, T., Karnauskas, K. B., & Radenac, M.-H. (2013). Biophysical responses near equatorial islands in the western Pacific ocean during El Niño/La Niña transitions. *Geophysical Research Letters*, *40*(20), 5473–5479. <https://doi.org/10.1002/2013gl057828>
- Gorgues, T., Menkes, C., Slemmons, L., Aumont, O., Dandonneau, Y., Radenac, M. H., et al. (2010). Revisiting the La Niña 1998 phytoplankton blooms in the equatorial Pacific. *Deep Sea Research Part I: Oceanographic Research Papers*, *57*(4), 567–576. <https://doi.org/10.1016/j.dsr.2009.12.008>
- Ham, Y.-G., Kug, J.-S., & Park, J.-Y. (2013). Two distinct roles of Atlantic SSTs in ENSO variability: North tropical Atlantic SST and Atlantic Niño. *Geophysical Research Letters*, *40*(15), 4012–4017. <https://doi.org/10.1002/grl.50729>
- Horowitz, L. W., Naik, V., Paulot, F., Ginoux, P. A., Dunne, J. P., Mao, J., et al. (2020). The GFDL global atmospheric chemistry-climate model AM4.1: Model description and simulation characteristics. *Journal of Advances in Modeling Earth Systems*, *12*(10), e2019MS002032. <https://doi.org/10.1029/2019ms002032>
- Hsu, N. C., Sayer, A. M., Jeong, M.-J., & Bettenhausen, C. (2013). *SeaWiFS Deep blue aerosol optical depth and Angstrom Exponent monthly level 3 data gridded at 1.0 Degrees V004*. Goddard Earth Sciences Data and Information Services Center (GES DISC).
- Huang, B., Thorne, P. W., Banzon, V. F., Boyer, T., Chepurin, G., Lawrimore, J. H., et al. (2017). Extended reconstructed sea surface temperature, version 5 (ERSSTv5): Upgrades, validations, and intercomparisons. *Journal of Climate*, *30*(20), 8179–8205. <https://doi.org/10.1175/jcli-d-16-0836.1>
- Jin, F.-F. (1997). An equatorial ocean recharge paradigm for ENSO. Part I: Conceptual model. *Journal of the Atmospheric Sciences*, *54*(7), 811–829. [https://doi.org/10.1175/1520-0469\(1997\)054<0811:aeorp>2.0.co;2](https://doi.org/10.1175/1520-0469(1997)054<0811:aeorp>2.0.co;2)
- Krasting, J., John, J., Blanton, C., McHugh, C., Nikonov, S., Radhakrishnan, A., et al. (2018). *NOAA-GFDL GFDL-ESM4 Model Output Prepared for CMIP6 CMIP* (Vol. 10). Earth System Grid Federation.
- Kug, J.-S., Choi, J., An, S.-I., Jin, F.-F., & Wittenberg, A. T. (2010). Warm pool and cold tongue El Niño events as simulated by the GFDL 2.1 coupled GCM. *Journal of Climate*, *23*(5), 1226–1239. <https://doi.org/10.1175/2009jcli3293.1>
- Kug, J.-S., Jin, F.-F., & An, S.-I. (2009). Two types of El Niño events: Cold tongue El Niño and warm pool El Niño. *Journal of Climate*, *22*(6), 1499–1515.
- Landry, M. R., Barber, R. T., Bidigare, R. R., Chai, F., Coale, K. H., Dam, H. G., et al. (1997). Iron and grazing constraints on primary production in the central equatorial Pacific: An EqPac synthesis. *Limnology & Oceanography*, *42*(3), 405–418. <https://doi.org/10.4319/lo.1997.42.3.0405>
- Le, T., Ha, K.-J., Bae, D.-H., & Kim, S.-H. (2020). Causal effects of Indian ocean Dipole on El Niño–Southern Oscillation during 1950–2014 based on high-resolution models and reanalysis data. *Environmental Research Letters*, *15*(10), 1040b1046. <https://doi.org/10.1088/1748-9326/abb96d>
- Le Borgne, R., Barber, R. T., Delcroix, T., Inoue, H. Y., Mackey, D. J., & Rodier, M. (2002). Pacific warm pool and divergence: Temporal and zonal variations on the equator and their effects on the biological pump. *Deep Sea Research Part II: Topical Studies in Oceanography*, *49*(13), 2471–2512. [https://doi.org/10.1016/s0967-0645\(02\)00045-0](https://doi.org/10.1016/s0967-0645(02)00045-0)
- Lee, K.-W., Yeh, S.-W., Kug, J.-S., & Park, J.-Y. (2014). Ocean chlorophyll response to two types of El Niño events in an ocean-biogeochemical coupled model. *Journal of Geophysical Research: Oceans*, *119*(2), 933–952. <https://doi.org/10.1002/2013jc009050>
- Lehodey, P., Alheit, J., Barange, M., Baumgartner, T., Beaugrand, G., Drinkwater, K., et al. (2006). Climate variability, fish, and fisheries. *Journal of Climate*, *19*(20), 5009–5030. <https://doi.org/10.1175/jcli3898.1>
- Le Page, Y., Pereira, J. M. C., Trigo, R., da Camara, C., Oom, D., & Mota, B. (2008). Global fire activity patterns (1996–2006) and climatic influence: An analysis using the World fire Atlas. *Atmospheric Chemistry and Physics*, *8*(7), 1911–1924.
- McClanahan, T. R., Darling, E. S., Maina, J. M., Muthiga, N. A., 'agata, S. D., Jupiter, S. D., et al. (2019). Temperature patterns and mechanisms influencing coral bleaching during the 2016 El Niño. *Nature Climate Change*, *9*(11), 845–851. <https://doi.org/10.1038/s41558-019-0576-8>
- McPhaden, M. J., Zebiak, S. E., & Glantz, M. H. (2006). ENSO as an integrating concept in earth science. *Science*, *314*(5806), 1740–1745. <https://doi.org/10.1126/science.1132588>

- Moore, J. K., Lindsay, K., Doney, S. C., Long, M. C., & Misumi, K. (2013). Marine ecosystem dynamics and biogeochemical cycling in the community earth system model [CESM1(BGC)]: Comparison of the 1990s with the 2090s under the RCP4.5 and RCP8.5 scenarios. *Journal of Climate*, 26(23), 9291–9312. <https://doi.org/10.1175/jcli-d-12-00566.1>
- Murray, J. W., Leinen, M. W., Feely, R. A., Toggweiler, J. R., & Wanninkhof, R. (1992). EqPac: A Process study in the central equatorial Pacific. *Oceanography*, 5(3), 134–142. <https://doi.org/10.5670/oceanog.1992.01>
- Ohba, M., & Ueda, H. (2007). An impact of SST anomalies in the Indian ocean in acceleration of the El Niño to La Niña transition. *Journal of the Meteorological Society of Japan Ser. II*, 85(3), 335–348.
- Park, J.-Y., Dunne, J. P., & Stock, C. A. (2018). Ocean chlorophyll as a precursor of ENSO: An earth system modeling study. *Geophysical Research Letters*, 45(4), 1939–1947. <https://doi.org/10.1002/2017gl076077>
- Park, J.-Y., Kug, J.-S., Park, J., Yeh, S.-W., & Jang, C. J. (2011). Variability of chlorophyll associated with El Niño–Southern Oscillation and its possible biological feedback in the equatorial Pacific. *Journal of Geophysical Research*, 116(C10). <https://doi.org/10.1029/2011jc007056>
- Park, J.-Y., Kug, J.-S., & Park, Y.-G. (2014). An exploratory modeling study on bio-physical processes associated with ENSO. *Progress in Oceanography*, 124, 28–41. <https://doi.org/10.1016/j.pocean.2014.03.013>
- Park, J.-Y., Kug, J.-S., Seo, H., & Bader, J. (2014). Impact of bio-physical feedbacks on the tropical climate in coupled and uncoupled GCMs. *Climate Dynamics*, 43(7–8), 1811–1827. <https://doi.org/10.1007/s00382-013-2009-0>
- Paulsen, H., Ilyina, T., Six, K. D., & Stemmler, I. (2017). Incorporating a prognostic representation of marine nitrogen fixers into the global ocean biogeochemical model HAMOCC. *Journal of Advances in Modeling Earth Systems*, 9(1), 438–464. <https://doi.org/10.1002/2016ms000737>
- Planton, Y. Y., Guilyardi, E., Wittenberg, A. T., Lee, J., Gleckler, P. J., Bayr, T., et al. (2021). Evaluating climate models with the CLIVAR 2020 ENSO metrics package. *Bulletin of the American Meteorological Society*, 102(2), E193–E217. <https://doi.org/10.1175/bams-d-19-0337.1>
- Racault, M.-F., Sathyendranath, S., Brewin, R. J. W., Raitsos, D. E., Jackson, T., & Platt, T. (2017). Impact of El Niño variability on oceanic phytoplankton. *Frontiers in Marine Science*, 4(133). <https://doi.org/10.3389/fmars.2017.00133>
- Radenac, M.-H., Léger, F., Singh, A., & Delcroix, T. (2012). Sea surface chlorophyll signature in the tropical Pacific during eastern and central Pacific ENSO events. *Journal of Geophysical Research: Oceans*, 117(C4). <https://doi.org/10.1029/2011jc007841>
- Salinas-de-León, P., Andrade, S., Arnés-Urgellés, C., Bermudez, J. R., Bucaram, S., Buglass, S., et al. (2020). Evolution of the Galapagos in the Anthropocene. *Nature Climate Change*, 10(5), 380–382.
- Sathyendranath, S., Jackson, T., Brockmann, C., Brotas, V., Calton, B., Chuprin, A., et al. (2020). *ESA Ocean Colour climate change Initiative (Ocean_Colour_cci): Global chlorophyll-a data products gridded on a sinusoidal projection. Version 4.2*. Centre for Environmental Data Analysis.
- Shao, Y., Klöse, M., & Wyrwoll, K.-H. (2013). Recent global dust trend and connections to climate forcing. *Journal of Geophysical Research: Atmospheres*, 118(19), 11–107. <https://doi.org/10.1002/jgrd.50836>
- Shiogama, H., Watanabe, M., Kim, H., & Hirota, N. (2022). Emergent constraints on future precipitation changes. *Nature*, 602(7898), 612–616. <https://doi.org/10.1038/s41586-021-04310-8>
- Stock, C. A., Dunne, J. P., Fan, S., Ginoux, P., John, J., Krasting, J. P., et al. (2020). Ocean Biogeochemistry in GFDL's earth system model 4.1 and its response to increasing atmospheric CO₂. *Journal of Advances in Modeling Earth Systems*, 12(10), e2019MS002043. <https://doi.org/10.1029/2019ms002043>
- Stock, C. A., Dunne, J. P., & John, J. G. (2014). Global-scale carbon and energy flows through the marine planktonic food web: An analysis with a coupled physical–biological model. *Progress in Oceanography*, 120, 1–28. <https://doi.org/10.1016/j.pocean.2013.07.001>
- Strutton, P. G., Evans, W., & Chavez, F. P. (2008). Equatorial Pacific chemical and biological variability, 1997–2003. *Global Biogeochemical Cycles*, 22(2). <https://doi.org/10.1029/2007gb003045>
- Stuecker, M. F., Timmermann, A., Jin, F.-F., McGregor, S., & Ren, H.-L. (2013). A combination mode of the annual cycle and the El Niño/Southern Oscillation. *Nature Geoscience*, 6(7), 540–544. <https://doi.org/10.1038/ngeo1826>
- Taylor, K. E., Stouffer, R. J., & Meehl, G. A. (2012). An overview of CMIP5 and the experiment design. *Bulletin of the American Meteorological Society*, 93(4), 485–498. <https://doi.org/10.1175/bams-d-11-00094.1>
- Tian, F., Rong-Hua, Z., & Xiujun, W. (2021). Indian Ocean warming as a potential trigger for super phytoplankton blooms in the eastern equatorial Pacific from El Niño to La Niña transitions. *Environmental Research Letters*.
- Timmermann, A., An, S. I., Kug, J. S., Jin, F. F., Cai, W., Capotondi, A., et al. (2018). El Niño–Southern Oscillation complexity. *Nature*, 559(7715), 535–545.
- Trenberth, K. E. (1997). The definition of El Niño. *Bulletin of the American Meteorological Society*, 78(12), 2771–2778. [https://doi.org/10.1175/1520-0477\(1997\)078<2771:tdoen>2.0.co;2](https://doi.org/10.1175/1520-0477(1997)078<2771:tdoen>2.0.co;2)
- Wilson, C., & Coles, V. J. (2005). Global climatological relationships between satellite biological and physical observations and upper ocean properties. *Journal of Geophysical Research: Oceans*, 110(C10). <https://doi.org/10.1029/2004jc002724>
- Wittenberg, A. T., Rosati, A., Lau, N.-C., & Ploshay, J. J. (2006). GFDL's CM2 global coupled climate models. Part III: Tropical Pacific climate and ENSO. *Journal of Climate*, 19(5), 698–722. <https://doi.org/10.1175/jcli3631.1>
- Woodward, F. I., Lomas, M. R., & Quaipe, T. (2008). Global responses of terrestrial productivity to contemporary climatic oscillations. *Philosophical Transactions of the Royal Society B: Biological Sciences*, 363(1504), 2779–2785. <https://doi.org/10.1098/rstb.2008.0017>
- Wyrtki, K. (1985). Water displacements in the Pacific and the genesis of El Niño cycles. *Journal of Geophysical Research: Oceans*, 90(C4), 7129–7132. <https://doi.org/10.1029/jc090ic04p07129>
- Yeh, S. W., Kug, J. S., Dewitte, B., Kwon, M. H., Kirtman, B. P., & Jin, F. F. (2009). El Niño in a changing climate. *Nature*, 461(7263), 511–514. <https://doi.org/10.1038/nature08316>
- Yoo, J.-H., Moon, S., Ha, K.-J., Yun, K.-S., & Lee, J.-Y. (2020). Cases for the sole effect of the Indian ocean Dipole in the rapid phase transition of the El Niño–Southern Oscillation. *Theoretical and Applied Climatology*, 141, 999–1007. <https://doi.org/10.1007/s00704-020-03265-6>
- Zhang, R.-H., Tian, F., & Wang, X. (2018). Ocean chlorophyll-induced heating feedbacks on ENSO in a coupled ocean physics–biology model forced by prescribed wind anomalies. *Journal of Climate*, 31(5), 1811–1832. <https://doi.org/10.1175/jcli-d-17-0505.1>
- Zhao, M., Golaz, J.-C., Held, I. M., Guo, H., Balaji, V., Benson, R., et al. (2018). The GFDL global atmosphere and land model AM4.0/LM4.0: 1. Simulation characteristics with prescribed SSTs. *Journal of Advances in Modeling Earth Systems*, 10(3), 691–734. <https://doi.org/10.1002/2017ms001208>
- Zhao, X., & NOAA-CDR-Program. (2017). *NOAA climate data record (CDR) of AVHRR daily and monthly aerosol optical thickness (AOT) over Global Oceans. Version 3.0 [indicate subset used]* NOAA National Centers for Environmental Information.